Ground-based remote sensing of O_3 by high and medium resolution FTIR spectrometers over the Mexico City basin

Eddy F. Plaza-Medina[1], Wolfgang Stremme[1], Alejandro Bezanilla[1], Michel Grutter[1], Matthias Schneider[2], Frank Hase[2], and Thomas Blumenstock[2]

[1]Centro de Ciencias de la Atmósfera, Universidad Nacional Autónoma de México, 04510 Ciudad de México, México
[2]Institute of Meteorology and Climate Research (IMK-ASF), Karlsruhe Institute of Technology, Karlsruhe, Germany

Correspondence to: E. F. Plaza-Medina and M. Schneider
(eddymedi@gmail.com and matthias.schneider@kit.edu)

Abstract. We present atmospheric ozone (O_3) profiles measured over central Mexico between November 2012 and February 2014 by two different ground-based FTIR (Fourier transform infrared) solar absorption experiments. The first instrument offers very high resolution spectra and contributes to NDACC (Network for the Detection of Atmospheric Composition Change). It is located at a mountain observatory about 1700 m above the Mexico City basin. The second instrument has a medium
5 spectral resolution and is located inside of Mexico City at a horizontal distance of about 60 km to the mountain observatory. It is documented that the retrieval with the high and medium resolution experiments give O_3 variations for three and four independent atmospheric altitude ranges, respectively, whereby the theoretically estimated errors of these profile data are mostly within 10%. The good quality of the data is empirically demonstrated: above the tropopause by intercomparing the two FTIR O_3 data and for the boundary layer by comparing the Mexico City FTIR O_3 data with in-situ O_3 surface data.
10 Furthermore, we develop a combined boundary layer O_3 remote sensing product that uses the retrieval results of both FTIR experiments and demonstrate theoretically and empirically the improvements achieved by such combination.

1 Introduction

O_3 is an important atmospheric trace gas. In the stratosphere O_3 absorbs ultraviolet (UV) radiation thereby protecting all living organisms. During the second half of the last century stratospheric ozone has experienced significant depletion. With the
15 implementation of the Montreal Protocol in 1987 and its amendments the anthropogenic emissions of the mainly responsible chlorine and fluoride compounds were strongly restricted and stratospheric O_3 depletion has progressively diminished (Scientific Assessment of Ozone Depletion, World Meteorological Organization, Pawson et al., 2014), and it is expected to become negligible by the end of this century (Hegglin and Shepherd, 2009). In the troposphere O_3 is an important pollutant and greenhouse gas (Jacob and Winner, 2009; Stock et al., 2014) and has increased since pre-industrial times (IPCC-2013, 2013). O_3 is
20 hazardous to human health and a severe problem in many cities around the globe as it is produced by complex photochemistry in presence of anthropogenic pollutants (NO_x, CO, and VOC) and UV radiation (e.g. Brasseur et al., 1999).

For understanding the stratospheric or tropospheric O_3 evolution the whole atmosphere has to be considered. For instance, Ramaswamy et al. (2006) showed that there is a correlation between the stratospheric cooling, stratospheric O_3 depletion and

the increase of greenhouse gases (mainly anthropogenic CO_2). Increases in tropospheric greenhouse gas concentrations warm the lower and middle troposphere and cool the stratosphere. The changed vertical temperature structure affects atmospheric dynamics and stratospheric O_3 distribution. The complexity of these interactions make it difficult to predict how, when, and to what extent stratospheric O_3 recovery will take place (Weatherhead and Andersen, 2006). Because tropospheric O_3 is a

5   greenhouse gas, increasing tropospheric O_3 levels will have an effect on the evolution of stratospheric O_3 concentrations. Similarly, tropospheric O_3 levels are influenced by the stratosphere and stratospheric O_3 concentrations in different ways. A direct connection exists during stratosphere-troposphere exchange events. Furthermore, stratospheric O_3 or aerosol loading affect the UV radiation penetrating to the troposphere and consequently the photochemistry of tropospheric O_3 and other species (Zhang et al., 2014).

10   A comprehensive investigation of these complex climate-chemistry interactions and the particular role of O_3 is only possible by combining atmospheric models with observations (Dameris and Jöckel, 2013; Hassler et al., 2013). In this context ground-based high resolution solar absorption FTIR spectrometer measurements have been proven to be useful, providing information of the vertical distribution of O_3 and other trace gases (e.g. Rinsland et al., 2003; Kohlhepp et al., 2012; Vigouroux et al., 2015; Barthlott et al., 2017). High resolution and high quality FTIR measurements are organised in the framework of NDACC and are

15   made at about 20 globally distributed sites (www.acom.ucar.edu/irwg/). Due to the high quality and long-term characteristics, the NDACC FTIR data are very interesting for trend studies (e.g. Kohlhepp et al., 2012; García et al., 2012; Vigouroux et al., 2015). However, the NDACC-like ground-based FTIR measurements are mainly performed at remote sites (i.e. far away from polluted areas) and very scarce in tropical latitudes. The only NDACC-like FTIR sites reporting atmospheric data within or close to the 20°N-20°S latitude belt are Mauna Loa (19.5°N, 155.6°W), Addis Ababa (9.0°N, 38.8°E, Takele Kenea et al.,

20   2013), Paramaribo (5.8°N, 55.2°W, Petersen et al., 2008) and La Réunion (21.1°S, 55.4°E, Senten et al., 2008). Medium resolution FTIR spectrometers have also been used to measure atmospheric O_3 amounts (e.g. over the megacity of Paris Viatte et al., 2011) however, a comprehensive quality documentation of the O_3 data retrieved from medium resolution FTIR spectra is still missing.

Here we present atmospheric O_3 profiles obtained from solar absorption spectra, measured by two different FTIR spec-

25   trometers in central Mexico (at about 19°N, 99°W). The first instrument is a high resolution FTIR spectrometer located at a high altitude station (Altzomoni), but very close to Mexico City. In the meanwhile these FTIR activities form part of NDACC and together with the Paramaribo measurements represent the only NDACC FTIR contribution from Latin America. The second instrument is a medium resolution FTIR spectrometer located inside of Mexico City, a megacity whose emissions have been investigated in great detail in the context of MILAGRO (Megacities Initiative: Local And Global Research Observations,

30   Molina et al., 2010, and references therein). We would like to point out that ground-based remote sensing measurements of the vertical O_3 distribution between the boundary layer and the upper stratosphere are challenged by the fact that the O_3 concentrations strongly vary with altitude. This is shown in the left panel of Fig. 1, which shows a typical tropical O_3 profile (blue line for volume mixing ratios and black for abundances relative to total abundances).

The focus of this paper is to demonstrate the reliability of the FTIR O_3 profiles between the boundary layer and the upper

35   stratosphere and in the following sections we will have a closer look on the altitude regions marked by yellow stars in the

left panel of Fig.1. Section 2 presents the high and medium resolution FTIR remote sensing experiments, the remote sensing retrievals and discusses the main characteristics of the retrieval products. In Sect. 3 we analyse the O_3 concentrations above the boundary layer and show that the total column amounts and lower and middle stratospheric O_3 amounts retrieved from the medium resolution FTIR measurements are in good agreement to the amounts retrieved from the high resolution FTIR

5   measurements. In Sect. 4 we investigate the possibility of observing O_3 concentrations in the boundary layer by the medium resolution FTIR instrument that is located in Mexico City. We empirically prove this possibility using boundary layer in-situ O_3 data as a reference and show that by combining the two remote sensing experiments we can generate a boundary layer O_3 remote sensing product with improved precision. Section 5 gives a summary and outlook.

2   Ground-based FTIR remote sensing

10   The right panel of Fig. 1 indicates the location of the two ground-based FTIR remote sensing and the three in-situ surface instruments that are used in the context of Sect. 4. The first FTIR instrument is located in Altzomoni within the Izta-Popo National Park at nearly 4000 m a.s.l. between the Popocatépetl and the Iztaccílhuatl volcanoes at 19.12°N, 98.65°W, about 1700 m above the Mexico City basin. The second instrument is located at the UNAM (Universidad Nacional Autónoma de México) in Mexico City, at the rooftop of the CCA (Centro de Ciencias de la Atmósfera, 19.33°N, 99.18°W, 2260 m a.s.l). The

15   UNAM stations is at a horizontal distance of about 60 km to Altzomoni in northwest direction and both stations are operated by the Spectroscopy and Remote Sensing Group of CCA/UNAM.

2.1   Experimental setup

A ground-based FTIR remote sensing experiment consists of a solar tracker and a Michelson-type interferometer. The solar tracker captures the direct solar light beam and couples it into the interferometer, which splits the solar light into two beams.

20   The first beam traverses a fixed distance and the second beam a variable distance. Finally the intensity of the recombined beam is analysed by a detector. In the middle infrared, where the here used two instruments are measuring, photo-conductive as well as photo-voltaic detectors are applied. The intensity of the recombined beam depend on their optical path difference and these intensity signals are called the interferogram. The spectrum is then calculated by a Fourier transformation of the interferogram.

The maximum optical path difference, the apodisation, and misalignments of the interferometer (which can be minimised but

25   not completely avoided) determine the instrumental line shape (ILS, the response of the instrument to a monochromatic input radiation). Understanding the ILS is important for correctly interpreting the measured spectra. The effect of misalignments on the ILS can be determined by low pressure gas cell measurements. Since the pressure and the absorption characteristics of the gas in the cell is known we can retrieve the ILS from such measurements (Hase, 2012).

2.2 Retrieval method

The measured solar absorption spectra (expressed as spectral bin vector y) and the atmospheric state (expressed by atmospheric state vector x) are connected via a radiative transport model (forward model F):

$$y = F(x,p). \tag{1}$$

5 Here the vector p represents auxiliary atmospheric parameters (like temperature) or instrumental characteristics (like the instrumental line shape). Generally, there are many different atmospheric states x that can equally well explain the measured spectrum y within its measurement noise level. This means that we face an ill-posed problem and we need to constrain the solution state. The constraint solution is at the minimum of the cost function:

$$[y - F(x,p)]^T S_\epsilon^{-1} [y - F(x,p)] + [x - x_a]^T S_a^{-1} [x - x_a]. \tag{2}$$

10 Here the first term is a measure of the difference between the measured spectrum (y with S_ϵ capturing the measurement noise covariance) and the spectrum simulated for a given atmospheric state (x). The second term is the regularisation term. It constrains the atmospheric solution state (x) towards the a priori state x_a, whereby the kind and the strength of the constraint are defined by the covariance matrix S_a. For more details about solving ill-posed problems in atmospheric remote sensing please refer to Rodgers (2000).

15 Since we face a non-linear problem the solution is reached iteratively, whereby for the $(i + 1)$ iteration's step it is:

$$x_{i+1} = x_a + S_a K_i^T (K_i S_a K_i^T + S_\epsilon)^{-1} [y - F(x_i) + K_i(x_i - x_a)]. \tag{3}$$

Here K is the Jacobian matrix which samples the derivatives $\partial y / \partial x$ (changes in the spectral radiances y for changes in the vertical distribution of the atmospheric constituents x).

An important addendum of the retrieved solution vector is the averaging kernel matrix A. It samples the derivatives $\partial x / \partial x_{act}$

20 (changes in the retrieved concentration x for changes in the actual atmospheric concentration x_{act}) describing the smoothing of the actual atmospheric state by the remote sensing measurement process:

$$(x - x_a) = A(x_{act} - x_a). \tag{4}$$

The matrix A can be calculated as:

$$A = GK = (KS_\epsilon^{-1}K^T + S_a^{-1})^{-1}K^T S_\epsilon^{-1}K. \tag{5}$$

25 Here G is the gain matrix, which samples $\partial x / \partial y$ (changes in the retrieved state x for changes in the spectral radiances y). The kernels are rather important since they document what is actually measured by the remote sensing system. Without this information, the remote sensing data cannot be used in a sensible manner. In addition, the trace of A quantifies the amount of information obtained by the measurement. It can be interpreted as the degrees of freedom of signal (DOFS) of the measurement.

In this study we work with the PROFFIT retrieval code (Hase et al., 2004), which has been used for many years by the

30 ground-based FTIR community for evaluating high resolution solar absorption spectra. PROFFIT offers three kind of constrains

for solving the inversion problem: scaling of a priori profiles, Optimal Estimation (using an $\mathbf{S_a}$ constructed from a model or measurement climatology, Rodgers, 2000) and Tikhonov-Phillips (using an ad-hoc created $\mathbf{S_a}^{-1}$ for constraining towards absolute profile values or the profile shape, Tikhonov, 1963; Rodgers, 2000).

We use a model atmosphere with 41 and 44 discretised grid levels from the surface up to 120 km for the Altzomoni and

5 UNAM retrievals, respectively, whereby the grid levels 1 to 3 of UNAM are situated below Altzomoni and the grid levels 4 to 44 of UNAM are the same as the grid levels 1 to 41 of Altzomoni. The O_3 inversions are regularised by a Tikhonov-Phillips constraint towards the vertical profile slope and towards the absolute value for the uppermost atmospheric model altitude (i.e. the 120 km grid level). The strength of the constraint is determined by starting with a weak constraint and then increasing it until a significant increase in the residual of the spectral fit is observed (L-curve criterion). The inversion is made

10 on the logarithmic scale of O_3 volume mixing ratios (Hase et al., 2004; Schneider et al., 2006). As a priori volume mixing ratio profiles (x_a) for O_3 and all interfering species we use climatologies from the Whole Atmosphere Community Climate Model (WACCM, version 6). The O_3 a priori profile is depicted in the left panel of Fig. 1. The temperature and pressure profiles are from the National Centers for Environmental Prediction (NCEP) analysis. For altitudes above 50 km we use monthly mean CIRA temperature climatologies (Rees et al., 1990). Spectroscopic line parameters for O_3 and interfering species are taken

15 from the High Resolution Transmission (HITRAN) 2008 database (Rothman et al., 2009), except for water, for which the HITRAN 2009 update is used.

2.3 Error analyses

The errors are estimated in form of a error covariance matrix $\mathbf{S_e}$:

$$\mathbf{S_e} = \mathbf{G K_p S_p K_p}^T \mathbf{G}^T. \qquad (6)$$

20 Here $\mathbf{G}$ is the gain matrix, $\mathbf{K_P}$ are the Jacobians with respect to the parameters p (changes of spectral bins due to changes in the parameters p) and $\mathbf{S_P}$ is the uncertainty covariance for the parameters p. We assume uncertainties for the parameters as listed in in Table 1, whereby assuming that the uncertainties between the different parameters are uncorrelated.

We consider a white noise in the measured spectra of 0.3% and 0.5% (ratio between noise and highest intensity in the measured spectral region), which is what we typically observe in the Altzomoni and UNAM spectra. As baseline channeling

25 amplitude we assume 0.2%, which is also what we occasionally observe in NDACC FTIR spectra measurements. We assume a relatively high baseline offset of 1% (higher than for other error assessment studies, e.g. Schneider and Hase, 2008), because in routine operations the spectra are often taken of sky that are partially covered by clouds. Generally, clouds cause very noisy measurements and can be easily identified. However, occasionally there might be clouds in the line of sight for a few seconds during a measurement (a measurement takes several minutes). Interferograms recorded during such intensity fluctuations then

30 lead to spectra with an increased baseline offset. For the ILS we assume an uncertainty in form of a linear decay of the modulation from the zero path difference to maximal optical path difference by 5% and for the phase error 0.1 rad for all positions of the interferometer mirror. The atmospheric temperature uncertainty from NCEP is assumed to be within 1.5 K (from the surface up to 45 km, whereby we separately consider tropospheric and stratospheric uncertainties) and 6 K for higher

altitudes. As uncertainty of the solar tracker we use 0.2°, which is a rather conservative estimate, since it is close to the radius of the solar disc (an error close to the radius of 0.25° would become clearly visible by high noise levels in the measured spectra). For estimating the effect of solar lines we work with the uncertainties that have been used in many other assessment studies (e.g. García et al., 2012). The spectroscopic parameters have typical uncertainties of 2 and 5% for line intensity and pressure

5   broadening, respectively (typical values as given in the HITRAN line parameter lists). Finally, we assume a 100% uncertainty in the atmospheric water vapour content. The large variability of tropospheric water vapour might affect the O_3 retrievals, even though the selected spectral windows contain only weak spectroscopic water vapour signatures.

2.4   Observations at Atzomoni

Infrared solar absorption spectra have been recorded at Altzomoni since May 2012 with a Bruker IFS 120/5HR spectrometer

10   (an IFS 120HR which has been upgraded with the electronics of an IFS 125HR). The sunlight is followed and guided to the spectrometer with a solar tracker, which is equipped with two plane ellipse-shape mirrors and two motors of rotation stage, one to access different elevation angles and the other to reach azimuthal directions. The pointing of the solar tracker is monitored and controlled with a standard CMOS USB-camera and the Camtracker software (Gisi et al., 2011). The solar tracker is protected with a motorized dome and the FTIR spectrometer and solar tracker are operated remotely from the UNAM

15   campus in Mexico City. The spectrometer allows measurements with very high resolution ($0.0035\,cm^{-1}$, i.e. maximum optical path difference of 257 cm) and is equipped with two beam-splitters: a potassium bromide (KBr, which is normally used) and a calcium fluoride (CaF_2, which is only occasionally used). Routine measurements are performed with three detectors: mercury-cadmium-teluride (MCT), indium-antimonide (InSb) and indium-gallium-arsenide (InGaAs). The first two are nitrogen-cooled and cover the spectral range of $700\text{-}4200\,cm^{-1}$ (mid-infrared region) and the third detector works at room temperature in the

20   spectral range $4000\text{-}12800\,cm^{-1}$ (near infrared region). In order to increase the signal to noise ratio in the mid-infrared spectral region, six NDACC-type filters are used to cover different spectral sub-regions. The Altzomoni FTIR experiment forms part of NDACC (www.ndacc.org) and also contributes to the MUSICA activities (Barthlott et al., 2017).

In order to investigate a potential misalignment of the interferometer and interpret the observed line shapes of the solar absorption spectra in a correct manner (Hase, 2012), we obtained the ILS from HBr cell measurements. This cell has a length

25   of 2 cm and is filled with HBr at a nominal pressure of 200 Pa (total pressure is between 200 to 250 Pa). The modulation and phase error of the ILS were calculated from the cell measurements using the LINEFIT code (Hase et al., 1999). The estimated ILS was then used for the retrieval process.

O_3 was retrieved from the solar absorption spectra obtained with the photo-conductive MCT detector, in the $750\text{-}1300\,cm^{-1}$ filter region at a spectral resolution of $0.005\,cm^{-1}$ and applying an aperture of 1.7 mm. Every spectrum is calculated from

30   averaging six scans with maximal resolution (total recording time of one spectrum is 12 minutes). Figure 2 gives an example of a typical measurement showing the five spectral windows that we use for the retrievals of O_3: $991.25\text{-}993.8\,cm^{-1}$, $1001.47\text{-}1003.04\,cm^{-1}$, $1005\text{-}1006\,cm^{-1}$, $1007.3\text{-}1009\,cm^{-1}$ and $1011.1\text{-}1013.6\,cm^{-1}$. These are the same windows as presented in Schneider and Hase (2008). We independently fit the $^{48}O_3$, the asymmetric $^{50}O_3$, the symmetric $^{50}O_3$ and all the $^{49}O_3$ isotopologues. All the O_3 isotopologues are fitted on a logarithmic volume mixing ratio scale. Furthermore, we perform

simultaneous fits on a linear volume mixing ratio scale of the interfering species H_2O, CO_2 and C_2H_4, which all have small signatures in the used spectral windows.

Figure 3 characterises the O_3 remote sensing data obtained at Altzomoni. The left panel shows the averaging kernels and the right panels the estimated uncertainty for the O_3 retrieval made with the typical FTIR measurement at Altzomoni as shown in Fig. 2. This measurement gives a DOFS value of 4.26, which is a typical value obtained for the Altzomoni O_3 retrievals. A DOFS of about 4.0 means that the O_3 values can be retrieved independently for about four different vertical altitude regions. For illustration, we highlight the row kernels for the retrievals at 4, 17, 28 and 42 km altitude by thick lines and different colours. The retrieval at 4 km is mainly influenced by actual atmospheric O_3 variations between 4 and 10 km (black line), the retrieval at 17 km by actual variations between 15 and 23 km (red line), the retrieval at 28 km by actual variations between 23 and 32 km (green line) and the retrieval at 42 km by actual variations between 32 and 45 km (blue line).

The estimated errors are depicted in the right panels of Fig. 3. Shown are the square root values of the diagonal elements of $\mathbf{S_e}$ calculated according to Eq. (6). Below the 30 km altitude total statistical and systematic errors are smaller than 5%. For higher altitudes the errors strongly increase and are larger than 10% above 40 km. Concerning the statistical error uncertainties, in temperature and baseline are the leading error sources, followed by uncertainties in the ILS and measurement noise. The systematic errors are dominated by uncertainties in the spectroscopic line parameters of O_3. Uncertainties in temperature, baseline and ILS are of secondary importance. Statistical and systematic errors due to uncertainties in the line of sight, solar lines and interferences with atmospheric H_2O variations are smaller than 0.1% throughout the atmosphere and are thus not depicted.

The errors for the total column abundances are listed in Table 2. They are calculated by applying the total column operator to the left and the transpose of the total column operator to the right of Eq. (6) and then taking the square root. The total column errors are between 2 and 3%, whereby the statistical error is mainly due to temperature uncertainty and the systematic error due to uncertainties in spectroscopic line intensity parameters of O_3.

For this work we analysed 1672 individual Altzomoni spectra, measured on 143 individual days between November 2012 and February 2014. We found that occasionally there are spectra with rather high noise levels, which then lead to retrievals with relatively low DOFS values. The high noise levels are caused probably by clouds that pass through the line of sight when recording the interferograms. The Fourier transformation of such interferogram would then lead to artefacts in the spectrum, like increased baseline offsets. In order to avoid that artefacts affect our study, we define as valid measurement only those for which the retrieval gives a DOFS value of at least 3.9, which is at the lower end of the DOFS values obtained for O_3 retrievals made with high resolution middle infrared solar absorption spectra (e.g. Schneider et al., 2008; García et al., 2012; Vigouroux et al., 2015). The DOFS filter leaves us with 1050 individual measurements made on 122 individual days between November 2012 and February 2014.

It is reasonable to assume that the Altzomoni solar absorption spectra are only very weakly affected by the polluted boundary layer. Most measurements are made before 14:00, when the boundary layer top altitude is below or weakly above the altitude of Altzomoni (Shaw et al., 2007; Baumgardner et al., 2009). Furthermore, very strong vertical mixing of air from below is generally linked to the presence of fog or clouds. Under such condition the FTIR is not operated.

2.5 Observations at UNAM

The UNAM atmospheric observatory is located in the South of Mexico City on the roof of the CCA, within the main UNAM campus. The infrared solar absorption spectral measurements started in 2008 using a Bruker Opag 22 spectrometer (measuring with spectral resolution of $0.5\,cm^{-1}$, Stremme et al., 2009). Since June 2010, spectra have been recorded with a Bruker Vertex

5   80 spectrometer allowing measurements with a maximum optical path difference of up to $12\,cm$, corresponding to a spectral resolution of $0.06\,cm^{-1}$. The spectrometer is equipped with a KBr beam splitter and two detectors (a nitrogen-cooled MCT detector and an InGaAs detector working at room temperature). In May 2012 we started to use four filters in the measurement routine, which cover different spectral sub-regions. The sunlight is guided by a solar tracker built in house which is covered with a motorized dome. For details see Bezanilla et al. (2014).

10   The spectra for the O_3 retrievals are measured with the photo-conductive MCT detector and with an aperture of $1.5\,mm$ using a long wave pass filter, which cuts on wavelength at $7.4\,\mu m$ (i.e. the filter is transparent for wavenumbers up to $1350\,cm^{-1}$). Every spectrum is obtained from averaging ten scans with a resolution of $0.1\,cm^{-1}$, stored every 12 seconds in the computer. For the retrievals we use one spectral window between 991 and $1073\,cm^{-1}$. Figure 4 shows the spectral window for a measurement that has been taken in temporal coincidence with the Altzomoni measurement shown in Fig. 2. It is the same spectral window

15   that has been used by Viatte et al. (2011). We fit the O_3 volume mixing ratios on a logarithmic volume mixing ratio scale, whereby all the different O_3 isotopologues are treated as a single species. As interfering species we simultaneously fit H_2O, CO_2, SO_2, NH_3 and C_2H_4, whereby we only allow for scaling of the prescribed first guess profiles (which are the same as the profiles used as a priori, i.e. from the WACCM climatology). Furthermore, we fit phase and amplitude of channeling with a frequency of $0.39\,cm^{-1}$ (this kind of channeling is what we occasionally observe in the UNAM spectra).

20   Figure 5 shows the averaging kernels and error estimations for the retrieval made with the measurement as shown in Fig. 4. The depicted row kernels belong to a averaging kernel matrix with a DOFS of 3.11, which is a typical value obtained for the UNAM O_3 retrievals and means that O_3 values can be retrieved independently for about three different vertical altitude regions. In Fig. 5 we highlight the row kernels corresponding to retrievals of the 2.3, 17 and $32\,km$ altitudes. The retrieval for $2.3\,km$ represents actual atmospheric O_3 variations between between 2.3 and $10\,km$, the retrieval for $17\,km$ the actual variations

25   between 15 and $24\,km$ and the retrieval for $32\,km$ the actual variations between 24 and $36\,km$. Even for spectra recorded with medium resolution the retrieval allows us to separate tropospheric, lower stratospheric and middle stratospheric O_3 variations.

Below $30\,km$ the O_3 errors estimated for UNAM are higher than the errors estimated for Altzomoni. We calculate total statistical and systematic errors of about 7.5%. The respective statistical errors are mainly controlled by uncertainties in the ILS, the baseline and the atmospheric temperatures. The respective systematic errors are dominated by uncertainties in the

30   spectroscopic line parameters of O_3, the ILS and the baseline. Above $30\,km$ the statistical errors increase to 10%, mainly caused by the increased importance of temperature uncertainties and measurement noise. The systematic errors slightly decrease to about 6% (above $30\,km$), mainly caused by decreasing importance of the uncertainties in the ILS and the baseline. Errors due to uncertainties of the line of sight, solar lines and interference with atmospheric H_2O variations are smaller than 0.1% throughout the atmosphere and not depicted.

The errors for the total column abundances are listed in Table 2. The respective UNAM errors are very similar to the Altzomoni errors (between 2 and 3%). As for Altzomoni the statistic error is mainly due to temperature uncertainty and the systematic error due to uncertainties in spectroscopic line intensity parameters of O_3.

For this work we analysed 1625 individual UNAM spectra measured on 88 individual days between November 2012 and

5 May 2013 (in June 2013 the measurements had to be interrupted due to construction works at UNAM). Similar to Altzomoni we filter the UNAM measurements with respect to the DOFS values obtained from the retrieval. We found that a DOFS value of 3.0 is a good threshold. Lower DOFS are strongly correlated to high noise levels and in particular to systematic residuals in the 1040-1045 cm^{-1} region. This DOFS filter leaves us with 717 individual measurements made on 65 individual days between November 2012 and May 2013.

10 ## 2.6 Logarithmic scale representation

In the equations and function (1)-(6) a logarithmic volume mixing ratio scale is used for the atmospheric O_3 state (we perform the O_3 retrieval on the logarithmic scale). In this context the errors as shown in Figs. 3 and 5 are from the logarithmic scale error covariance matrix $\mathbf{S_e}$ according to Eq. (6), i.e. they represent actually errors in the logarithm of the O_3 volume mixing ratio. We interpret these logarithmic scale errors as relative errors, because $d\ln x = \frac{dx}{x}$ and $\Delta\ln x \approx \frac{\Delta x}{x}$.

15 Throughout the paper we will use differentials or differences in the logarithms of O_3 as equivalent to relative O_3 differentials or differences: like in this section in the context of error assessment studies and also in the following sections when comparing two different data sets. For the latter the differences in the logarithms of the two data sets will be calculated and then interpreted as relative differences.

3 Free tropospheric and stratospheric O_3

20 In this section we analyse the O_3 variations that are not linked to ozone smog events. To do so we work with free tropospheric O_3 data measured outside Mexico City and with stratospheric O_3 data. First we discuss the seasonal cycles as observed above Altzomoni and then demonstrate to what extent the stratospheric O_3 variations can also be observed from the medium resolution instrument that is located in the Mexico City boundary layer.

3.1 Seasonal cycle above Altzomoni

25 Figure 6 depicts the monthly averages of O_3 total column amounts (top panel) and volume mixing ratios for different altitudes (bottom panel) for the months where there are at least Altzomini FTIR measurements on three different days. The error bars indicate the standard error of the mean, which is the standard deviation divided by the square root of the number of measurements used when calculating the mean value. The volume mixing ratios are presented for the altitudes whose row kernels are highlighted in the left panel of Fig. 3. The seasonal variation at the different altitudes is shown in a single graph, but

30 with different volume mixing ratio scale. The data points and the corresponding volume mixing ratio scales can be identified by different colours: dark gray for 4 km, red for 17 km, green for 28 km and blue for 42 km.

The seasonal cycle of the O_3 total column amounts above Altzomoni is rather smooth with a maximum in summer (in August 2013 almost 290 DU is reached) and a minimum in January (the January average is 241 DU). This is significantly different to the seasonal cycles of O_3 total column amounts as observed over subtropical, mid-latitudinal and polar sites. There the maximum is reached in spring and the minimum in autumn (e.g. Vigouroux et al., 2015). A look on the seasonal cycles for

5   different altitudes can help to understand the particularity of the seasonal O_3 distributions over central Mexico.

In the free troposphere (represented by the 4 km retrievals) there seems to be two clearly distinguishable periods. A winter period from November to February with O_3 values of about 0.04 ppmv and a second period from April to August with O_3 values between 0.05 and 0.06 ppmv. This is similar to the seasonal cycle of mid-latitudinal and subtropical tropospheric O_3 found for the two high altitude stations Izaña and Jungfraujoch (García et al., 2012; Vigouroux et al., 2015). In an exemplary

10 study for 2006, Thompson et al. (2008) found that most of this spring-to-summer increase over central America occurs between 5 and 12 km altitude. They attributed the increased tropospheric background O_3 levels to accumulation of earlier stratospheric O_3 input and to more O_3 pollution being imported from lower altitudes. The importance of the Mexico City emissions on free tropospheric O_3 levels in the surroundings of Mexico City has also been demonstrated in the context of the model study of Emmons et al. (2010).

15 In the upper troposphere and lower stratosphere (UTLS, represented by the 17 km retrievals) the seasonal variation is smoother and there is a slow but consistent gradual increase of O_3 concentrations between January and August. Unfortunately we have not a significant number of observations in September and October, but the August, November and December data seem to suggest a gradual decrease between August and December/January. The maximum in late summer and the minimum in winter is very different to what has been observed at other sites (Vigouroux et al., 2015), where the seasonal cycle of the UTLS

20 is strongly linked to the seasonal variation of the tropopause height. Between the subtropics and polar regions the tropopause is highest at the end of the summer and lowest in winter/spring, resulting in low UTLS O_3 volume mixing ratios in summer and high ratios in winter. Above Altzomoni it is the other way round. The reason is the importance of isentropic mixing of O_3 rich air from higher latitudes into the UTLS above Altzomoni. This mixing is strongest in summer and is also seen in space-based observations (Stolarski et al., 2014). Shuckburgh et al. (2009) investigated the longitudinal, seasonal and interannual variations

25 of these mixing events and showed that the mixing is strongest in the northern hemispheric summer and close to the Asian and North American monsoon regions. Furthermore, they found in particular strong mixing for negative ENSO (El Niño Southern Oscillation) years. Isentropic mixing may be determining the seasonal signal in the UTLS region also affecting the seasonal cycle of the total column amounts in central Mexico, but this needs to be further investigated. Long-term FTIR measurements at Altzomoni, which is situated in the North American monsoon region, will allow to study these stratosphere-troposphere

30 exchange processes and their link to climate patterns like ENSO.

In the middle stratosphere (represented by the 28 km retrievals) we observe an increase between January and May and a decrease between May and November, i.e. the maximum values are already achieved in May. For the retrieval at 42 km (representative for the middle and upper stratosphere), we observe a maximum in late summer and a minimum in winter. These middle and upper stratospheric cycles at Altzomoni are similar to the cycles as observed at the subtropical site of Izaña

35 (García et al., 2012).

3.2 Intercomparison between UNAM and Altzomoni data

When comparing different remote sensing products we have to consider the respective averaging kernels. The kernels as depicted in Figs. 3 and 5 reveal that at Altzomoni we can observe more details of the vertical O_3 distribution as compared to UNAM. Therefore before comparing the Altzomoni and the UNAM retrieval products we have to account for this difference

5   by smoothing the retrieved Altzomoni O_3 state vector ($\boldsymbol{x}_{\mathrm{ALTZ}}$) with the UNAM averaging kernel ($\mathbf{A}_{\mathrm{UNAM}}$).

$$\boldsymbol{x}^*_{\mathrm{ALTZ}} = \mathbf{A}_{\mathrm{UNAM}}(\boldsymbol{x}_{\mathrm{ALTZ}} - \boldsymbol{x}_{\boldsymbol{a}\,\mathrm{ALTZ}}) + \boldsymbol{x}_{\boldsymbol{a}\,\mathrm{ALTZ}}. \tag{7}$$

Here the vectors $\boldsymbol{x}_{\mathrm{ALTZ}}$ and $\boldsymbol{x}_{\boldsymbol{a}\,\mathrm{ALTZ}}$ have been expanded by three additional dimensions, which correspond to the three altitude grid levels below 4 km. For these three grid levels we set $\boldsymbol{x}_{\mathrm{ALTZ}} = \boldsymbol{x}_{\boldsymbol{a}\,\mathrm{ALTZ}} = \boldsymbol{x}_{\boldsymbol{a}\,\mathrm{UNAM}}$.

Applying Eq. (7) makes the data better comparable but does not fully remove the effect of the different averaging kernels.

10   In order to assure that we perform a reasonable comparison we calculate the covariance $\mathbf{S}_{\mathbf{cmp}}$ that estimates the comparability between the UNAM remote sensing data and the Altzomoni remote sensing data after smoothing according to Eq. (7):

$$\mathbf{S}_{\mathbf{cmp}} = (\mathbf{A}_{\mathrm{UNAM}} - \mathbf{A}_{\mathrm{UNAM}}\mathbf{A}_{\mathrm{ALTZ}})\mathbf{S}_{\mathbf{cov}}(\mathbf{A}_{\mathrm{UNAM}} - \mathbf{A}_{\mathrm{UNAM}}\mathbf{A}_{\mathrm{ALTZ}})^{T}. \tag{8}$$

whereby $\mathbf{A}_{\mathrm{UNAM}}$ is the averaging kernel matrix for UNAM and $\mathbf{A}_{\mathrm{ALTZ}}$ the averaging kernel matrix for Altzomoni, being expanded by three columns and three rows with 0.0 entries corresponding to the three altitude grids below 4 km altitude. The

15   matrix $\mathbf{S}_{\mathbf{cov}}$ describes the O_3 covariances in the atmosphere. Here we use an $\mathbf{S}_{\mathbf{cov}}$ calculated by assuming 100% O_3 variability throughout the atmosphere and a correlation length of 5 km. For a reasonable comparison we require that the square root of the diagonal of $\mathbf{S}_{\mathbf{cmp}}$ that represents the altitude under consideration is smaller than 10%.

Figure 7 shows a comparison the total column amounts as well as for volume mixing ratios at 17 km and 32 km a.s.l. after applying the smoothing from Eq. (7) and the aforementioned filtering. We pair UNAM and Altzomoni data that are measured

20   within 2h and then calculate the hourly means for all the pairs. This gives 66 individual data pairs that belong to measurements made on 29 individual days and during 7 different months from November 2012 to May 2013.

The total columns are calculated from the retrieved UNAM profiles (state vector $\boldsymbol{x}_{\mathrm{UNAM}}$) and the retrieved and smoothed Altzomoni profiles (state vector $\boldsymbol{x}^*_{\mathrm{ALTZ}}$, according to Eq. 7). As documented by the left graph of Fig. 1 about 97% of the O_3 total column abundances as measured at UNAM are situated above the altitude of Altzomoni and indeed we observe a

25   very good correlation between the data from both stations (a correlation coefficient R^2 of 96% and a slope m for the linear regression line of 1.06). The mean difference (UNAM − Altzomoni) is +2.0% and the 1σ scatter is 1.2%. The bias of +2.0% is in good agreement to the typical relative O_3 abundances between 2.3 and 4 km (see black line in the left panel of Fig. 1).

The correlations between the volume mixing ratios obtained at 17 km are also strong (R^2 of 86%). However the slope of the regression line is significantly larger than unity ($m = 1.22$). For the mixing ratios at 32 km the correlation is a bit weaker,

30   although still clearly observable (R^2 is 75%), and the slope of the regression line is close to unity ($m = 0.94$). The mean differences and scatter (UNAM − Altzomoni) are +8.7%±5.2% for 17 km and −2.1%±2.1% for 32 km, respectively.

4 Boundary layer

This section focuses on the O_3 volume mixing ratios in the boundary layer of the Mexico City basins, whose variations are driven mainly by photochemistry from anthropogenic pollutants (photochemical ozone smog).

4.1 In-situ monitoring of air pollution in Mexico City

5 For validating the boundary layer remote sensing product we use in situ measurements made in Mexico City in the framework of the RAMA (Red Automática de Monitoreo Atmosférico) network. RAMA performs continuous measurements of different gases and particles in 34 stations spread around Mexico City in order to give information about air quality of this megacity (more details about RAMA are available at www.aire.df.gob.mx/default.php).

The in-situ O_3 monitoring data are freely available with an hourly time resolution. We work with the three in-situ stations
10 Pedregal (PED), Santa Ursula (SUR) and Coyoacan (COY), which are all situated within a circle of about 5 km radius around the UNAM station, thereby constituting an excellent reference for assessing the potential of the UNAM remote sensing experiment for observing boundary layer O_3 mixing ratios. We calculate the mean value from the three stations for each hour and only consider situations where all three stations provide data.

Figure 8 depicts the monthly means of the diurnal cycles obtained from these three in-situ stations and represents the
15 known O_3 variability with highest monthly surface averages during the March-May months. It is during this period that the city suffers the largest number of exceedances and that the government activates the contingency plans for minimizing the high O_3 pollution episodes. The observed high diurnal variability, which is evidently larger than the seasonal variability, reveals the photochemical nature and reactivity of this urban atmosphere. The blue dots depict the time period when the FTIR measurements are typically performed (between 11 and 14 local time). Within these three hours O_3 concentrations show a
20 strong increase. Any comparison study has to consider these fast changing O_3 concentrations and we only compare data that are measured within the same hour. A discussion on O_3 boundary layer variability of Mexico City on time scales beyond the diurnal time scale is given in Barrett and Raga (2016).

4.2 Intercomparison of remote sensing data with in-situ data

For the comparison between the in-situ and remote sensing data, we require that during a certain hour (given in local time) all
25 the three experiments provide at least one measurement. We created a table that contains the data from the three experiments for these coincidences and then calculated the hourly mean data. This gives 36 individual hourly mean data triplets belonging to measurements made during 18 individual days during 6 different months (between November 2012 and April 2013).

Figure 9 shows the correlation plots between the O_3 in-situ data (measured in the Mexico City boundary layer at about 2.3 km a.s.l.) and the O_3 values obtained for the lowermost altitude for the retrievals at Altzomoni and UNAM. The left panel
30 depicts the correlation between the in-situ data and the Altzomoni retrieval product for 4 km a.s.l.. We observe no correlation ($R^2 < 1\%$) and a mean difference and 1σ standard deviation of the difference of -38.0%±31.3% (for Altzomoni − In-situ). This is not surprising given the significant horizontal distance between the location of the in-situ instruments and Altzomoni

and the fact the Altzomoni data have no sensitivity below 4 km a.s.l.. This implies that the variation as observed by the in-situ instruments are rather local and vertically and/or horizontally limited to the area around the in-situ instruments (or the basin of Mexico City).

The middle panel of Fig. 9 presents the correlation between the same in-situ data and the UNAM retrieval product for 2.3 km a.s.l.. There is a clear correlation between the two data sets ($R^2 = 66\%$), although the UNAM FTIR data do not fully capture the magnitude of the O_3 variability at the surface (slope m of the linear regression line is only 0.49). A slope of below 0.5 is actually what can be expected from the respective averaging kernels. The thick black line in Fig. 10 depicts the row kernel for the UNAM retrieval at 2.3 km. Summing up all the contributions of the row kernel for the boundary layer (values between surface and 4 km a.s.l.) we get about 0.35. If we assume that the diurnal O_3 increase is present throughout the entire boundary layer and if we further assume that it is stronger a few hundred meters above the surface (compared to the increase as observed in the mean values of the three in-situ stations), we can expect a slope above 0.35. Between 9:00 and 14:00 local time such assumption is reasonable, judging from the vertical O_3 profiles shown in Velasco et al. (2008) and the depth of the boundary layer (Shaw et al., 2007). The mean difference and 1σ standard deviation of the difference is +1.2%±17.9% (for UNAM − In-situ)

The good agreement with the in-situ data empirically proves the profiling capability of the UNAM FTIR experiment: it is able to detect the O_3 variations that take place in the Mexico City boundary layer, although it is a relatively thin layer containing only a small portion of the total column O_3 abundance above UNAM (see left panel in Fig. 1).

4.3 A combined UNAM/Altzomoni remote sensing product for the boundary layer

We have two remote sensing experiments located close to each other but at different altitudes. In this section we present a product that combines the measurement made by the two instruments. The objective is to investigate if the combination can improve the remote sensing boundary layer data.

A simple method is to calculate the differences between the total columns measured above UNAM and above Altzomoni, i.e. the differences of the total columns values as depicted in the left panel of Fig. 7. However, we have to consider that the partial column between 2.3 km and 4 km is only about 2.5% of the total column amount (see left panel of Fig. 1). Even after treating the Altzomoni data with the UNAM kernel (according to Eq. 7) the UNAM and the Altzomoni total column have still not the same sensitivity. Actually if we use the metric as described in the context of Eq. (8) we find that the partial columns above 4 km altitude can typically agree only within 0.9%. A better agreement cannot be expected due to the different sensitivities of the two remote sensing experiments. In addition there are errors in the total column amounts, which are estimated to 2.5-3% for each of the two experiments (see Table 2). In summary, the difference between the two column amounts is affected by different sensitivities and errors, whereby both effects together sum up to about 4-5%. This is larger than the expect value for the difference of about 2.5% and in addition it has to be consider that the boundary layer sensitivity is only 35% (sum of the diagonal elements of the averaging kernel corresponding to boundary layer altitudes, see discussion in the context of Fig. 9, middle panel). We cannot expect detecting a 2.5%×35%<0.9% signal by a measure that has an uncertainty of 4-5% and in consequence the difference of the total column amounts cannot give useful information about the partial column between

2.3 km and 4 km. Actually, we have calculated the total column amount differences and find indeed no correlation to the boundary layer in-situ data.

We need a more sophisticated method for combining the two experiments. We can start with the UNAM product at 2.3 km, which shows correlations to the boundary layer in-situ data (recall middle panel of Fig. 9). The typical row kernel for the

5 UNAM retrieval at 2.3 km is depicted as thick black line in Fig. 10. The kernel indicates some sensitivity for altitudes at and below 4 km, although the sum of the diagonal elements of the kernel corresponding to these altitudes is typically 0.35, i.e. significantly smaller than 1.0. It can also be seen that the 2.3 km retrieval is sensitive to the actual atmosphere above 4 km (the row kernel values only slowly decrease for altitudes above 4 km), i.e. free tropospheric O_3 variations can significantly interfere with the boundary layer variations. Our idea is to improve the sensitivity for the boundary layer and at the same time

10 reduce the interferences from higher altitudes by combining the UNAM measurements with the Altzomoni measurements. The Altzomoni data are promising for reducing the interferences because it is sensitive to the free troposphere above 4 km, but completely insensitive to the boundary layer below 4 km (see the row averaging kernel for the Altzomoni retrieval at 4 km depicted as thick grey line in Fig. 10).

4.3.1 Analytical description of the combined product

15 We introduce an operator $\mathbf{C}$ for combining the two retrievals:

$$\mathbf{C} = \frac{1}{\sum\limits_{i \, \epsilon \, \mathrm{BL}} a_{\mathrm{comb}}(i,i)} \left(\begin{array}{cc} \mathbb{I} & -\mathbf{A}_{\mathrm{UNAM}} \end{array} \right). \tag{9}$$

Here $\mathbb{I}$ is a $nol \times nol$ identity matrix and $\mathbf{A}_{\mathrm{UNAM}}$ the $nol \times nol$ averaging kernel matrix for UNAM, whereby nol is the number of grid points of the model atmosphere used for the UNAM retrieval process (i.e. here $nol = 44$). So $\mathbf{C}$ is a $nol \times (2 \times nol)$ matrix. The matrix is normalised to $\sum_{i \epsilon \mathrm{BL}} a_{\mathrm{comb}}(i,i)$, where $a_{\mathrm{comb}}(i,i)$ are the diagonal elements of $\mathbf{A}_{\mathrm{comb}}$ and $i \epsilon \mathrm{BL}$ are the

20 indices for the altitudes at and below 4 km (i.e. the boundary layer, BL). The matrix $\mathbf{A}_{\mathrm{comb}}$ is calculated according to Eq. (11), so for calculating $\mathbf{A}_{\mathrm{comb}}$ we actually need the operator $\mathbf{C}$, which in its turn needs diagonal elements from matrix $\mathbf{A}_{\mathrm{comb}}$. So we need two iterations to calculate $\mathbf{C}$ and $\mathbf{A}_{\mathrm{comb}}$ correctly: first we apply Eq. (9) using 1.0 for the normalisation, then we apply $\mathbf{A}_{\mathrm{comb}}$ according to Eq. (11). This gives us the correct normalisation factor for calculating the correct operator $\mathbf{C}$.

With the combination operator $\mathbf{C}$ the combined product can be calculated and comprehensively characterised in a similar

25 way as the individual products. The combined state vector $\boldsymbol{x}_{\mathrm{comb}}$ can be calculated from the UNAM and Altzomoni state vectors ($\boldsymbol{x}_{\mathrm{UNAM}}$ and $\boldsymbol{x}_{\mathrm{ALTZ}}$, respectively) as follows:

$$\boldsymbol{x}_{\mathrm{comb}} = \mathbf{C} \left[\left(\begin{array}{c} \boldsymbol{x}_{\mathrm{UNAM}} \\ \boldsymbol{x}_{\mathrm{ALTZ}} \end{array} \right) - \left(\begin{array}{c} \boldsymbol{x}_{\boldsymbol{a}\,\mathrm{UNAM}} \\ \boldsymbol{x}_{\boldsymbol{a}\,\mathrm{ALTZ}} \end{array} \right) \right] + \boldsymbol{x}_{\boldsymbol{a}\,\mathrm{UNAM}}. \tag{10}$$

Here $\boldsymbol{x}_{\boldsymbol{a}\,\mathrm{UNAM}}$ and $\boldsymbol{x}_{\boldsymbol{a}\,\mathrm{ALTZ}}$ are the a priori state vectors for UNAM and Altzomoni, which are identical. As for Eq. (7) the Altzomoni state vectors are expanded to 44 dimensions and we define $\boldsymbol{x}_{\mathrm{ALTZ}} = \boldsymbol{x}_{\boldsymbol{a}\,\mathrm{ALTZ}} = \boldsymbol{x}_{\boldsymbol{a}\,\mathrm{UNAM}}$ for the three vector

30 components corresponding to the three altitude levels below 4 km.

The averaging kernel for the combined product can be calculated as:

$$\mathbf{A}_{\text{comb}} = \mathbf{C} \begin{pmatrix} \mathbf{A}_{\text{UNAM}} \\ \mathbf{A}_{\text{ALTZ}} \end{pmatrix}. \tag{11}$$

Here the matrix $\mathbf{A}_{\text{ALTZ}}$ is the same as in Eq. (8), i.e. the original averaging kernel matrix of Altzomoni expanded by three columns and three rows with 0.0 entries corresponding to the three altitude grids below 4 km altitude (this gives a $nol \times nol$
5   matrix).

Similarly to Eq. (6) we can calculate error covariances for the combined product:

$$\mathbf{S}_{\mathbf{e},\text{comb}} = \mathbf{C} \begin{pmatrix} \mathbf{G}_{\text{UNAM}} & 0 \\ 0 & \mathbf{G}_{\text{ALTZ}} \end{pmatrix} \begin{pmatrix} \mathbf{K}_{\mathbf{p},\text{UNAM}} & 0 \\ 0 & \mathbf{K}_{\mathbf{p},\text{ALTZ}} \end{pmatrix} \begin{pmatrix} \mathbf{S}_{\mathbf{p},\text{UNAM}} & \mathbf{S}_{\mathbf{p},\text{x}} \\ \mathbf{S}_{\mathbf{p},\text{x}} & \mathbf{S}_{\mathbf{p},\text{ALTZ}} \end{pmatrix}$$
$$\begin{pmatrix} \mathbf{K}_{\mathbf{p},\text{UNAM}}{}^{T} & 0 \\ 0 & \mathbf{K}_{\mathbf{p},\text{ALTZ}}{}^{T} \end{pmatrix} \begin{pmatrix} \mathbf{G}_{\text{UNAM}}{}^{T} & 0 \\ 0 & \mathbf{G}_{\text{ALTZ}}{}^{T} \end{pmatrix} \mathbf{C}^{T}. \tag{12}$$

Here the matrix $\mathbf{G}_{\text{ALTZ}}$ is the original gain matrix for Altzomoni expanded by three lines (corresponding to the three altitude
10   grid levels below 4 km) to nol lines. The entries in these lines are 0.0. The matrices $\mathbf{K}_{\mathbf{p},\text{UNAM}}$ and $\mathbf{K}_{\mathbf{p},\text{ALTZ}}$ are the Jacobians with respect to parameter p and the matrices $\mathbf{S}_{\mathbf{p},\text{UNAM}}$ and $\mathbf{S}_{\mathbf{p},\text{ALTZ}}$ give the the uncertainty covariances for parameters p for the UNAM and the Altzomoni retrievals, respectively. The block $\mathbf{S}_{\mathbf{p},\text{x}}$ define the correlation between uncertainties for UNAM and Altzomoni. Here we assume that all uncertainties are uncorrelated, except for the temperature uncertainties above 12.5 km, for which we assume full correlation (i.e. $\mathbf{S}_{\mathbf{p},\text{x}}$ has only entries for the elements that correspond to temperature uncertainties
15   above 12.5 km). In the troposphere we assume that the uncertainty in the temperatures above UNAM and Altzomoni are uncorrelated, because here small scale variation are likely. For altitudes above 12.5 km we assume correlated temperature uncertainties because at these altitudes the variations on smaller scales are less likely. In this context please be aware that for both sites we assume the same temperatures, which are from NCEP and climatology of CIRA for altitudes above 50 km.

4.3.2 Discussion

20   The row of $\mathbf{A}_{\text{comb}}$ corresponding to 2.3 km is depicted as thick red line in Fig. 10 and indicates that, in comparison to the UNAM product, the combined retrieval product has much larger sensitivity in the boundary layer but at the same time much less sensitivity to variations that occur above 4 km. In this context our approach using two remote sensing experiments observing at different altitudes seems to be very promising.

However, we also have to consider the errors. By combining two measurements we increase the errors because the errors of
25   the two measurements are largely independent. In addition, by using the normalisation factor we make the data more sensitive to actual atmospheric variations, but also to uncertainty sources. Table 3 collects the errors estimated for the UNAM and the combined product at 2.3 km altitude. The values are the square roots of the diagonal entries of $\mathbf{S}_{\mathbf{e}}$ and $\mathbf{S}_{\mathbf{e},\text{comb}}$, according to Eqs. (6) and (12), respectively, that correspond to the altitude of 2.3 km. Because we assume that the UNAM and Altzomoni uncertainties are uncorrelated (except for temperatures uncertainties above 12.5 km) and because we increase the sensitivity

(by using the normalisation factor), the errors are significantly larger in the combined product than in the UNAM product. We estimate that the total statistical and systematic errors can be as large as 30%. So while the combination strongly reduces interferences from O_3 variations above 4 km and increases the sensitivity to actual boundary layer O_3 variations, it significantly increases the errors by summing up error contributions from two different experiments and by increasing the sensitivity to all

5 uncertainty sources.

In the right panel of Fig. 9 we compare the combined product with the in-situ data (for exactly the same coincidences that are shown in the other panels). We find that the combined product clearly correlates better with the in-situ data than the UNAM product (R^2 increases from 66% to 79%). The slope m does increase significantly, which is achieved by the normalisation factor when calculating $\mathbf{C}$ according to Eq. (9). The normalisation factor assures that for the combined product the DOFS for the

10 boundary layer is 1.0. This result is a clear empirical evidence that by combining the solar absorption spectra measurements of UNAM and Altzomoni according to Eq. (10), we can generate data that well capture the variations taking place in the Mexico City boundary layer. However, at the same time we observe a significant bias with respect to the in-situ data. The mean difference and 1σ standard deviation of the difference is +62.8%±16.5% (Combined − In-situ). The bias is more than twice as high as the estimated total systematic error from Table 3.

15 There can be different reasons for this unexpected large bias. It might be that we underestimate the systematic errors by assuming too low uncertainties in the spectroscopic line parameter data of O_3. For instance by assuming 20% (instead of 5%) uncertainty in the pressure broadening parameters for any of the both retrievals (UNAM or Altzomoni) could explain a systematic error of 60%. Furthermore, it might be that the boundary layer sensitivity of the UNAM retrieval is incorrectly captured by not considering O_3 continuum absorptions (for the UNAM we use a broad spectral window and O_3 continuum

20 absorptions might be important). On the other hand at least part of the systematic difference between the in-situ and the remote sensing data might be explained by the fact that the two measurement techniques observe different air masses. The in-situ instruments detect air at 2-5 m above the surface, while the remote sensing data represent the first 2 km above the surface. In model studies (e.g. Raga and Raga, 2000) as well as from observations (e.g. Velasco et al., 2008; Thompson et al., 2008), increased O_3 concentrations have been found about 1 km above the surface. This increase from the surface up to 1 km

25 above the surface seems to be particularly important in the morning and disappears at midday (Velasco et al., 2008). So when interpreting the differences between the in-situ and remote sensing data we have to keep in mind that both data represent different altitude regions. Actually this makes the remote sensing data especially interesting: they complement the in-situ data by giving information about a 2 km thick layer above the surface, and thus opening the possibility to detect extraordinary enhancements such as in Bezanilla et al. (2014), or the possibility to quantify a residual layer within the boundary layer as is

30 suggested in this study.

5 Summary and outlook

To our knowledge we present the first ground-based FTIR remote sensing data of O_3 profiles for Latin America. We work with two different FTIR experiments located one in the megacity of Mexico City and another about 1700 m above the city at a

distance of 60 km. The instrument in the city is a moderate resolution instrument and is installed on the top of a building at the main UNAM campus. The instrument outside the city is a high resolution instrument, situated on the high altitude observatory of Altzomoni and contributes to the NDACC (currently it is the highest NDACC FTIR station worldwide).

It is demonstrated that with the high altitude NDACC instrument one can typically detect the O_3 volume mixing ratio
5   variations of four different altitude regions: the free troposphere, the UTLS, the middle stratosphere and the middle/upper stratosphere. This is in agreement to other sites for which ground-based FTIR remote sensing profiles of O_3 have been characterised. We found that the error in the profiles are typically within 5% except for altitudes above 30 km, where they can reach 10-20%. Statistic errors are dominated by uncertainties in the used atmospheric temperature profiles and systematic errors are mainly due to uncertainties in the spectroscopic line parameters of O_3. These results are in agreement to previous error
10   estimations studies for NDACC FTIR O_3 data retrievals at other stations.

We show a first error estimation for O_3 profiles obtained for retrievals that use moderate resolution solar absorption spectra (the UNAM measurements). The estimated profile errors are below 10% between surface and 50 km, being dominated by uncertainties in atmospheric temperature (statistical error) and uncertainties baseline of the measured spectra and the spectroscopic line parameters of O_3 (systematic error). It is documented that remote sensing with the moderate resolution instruments
15   still allows for detecting three different altitude regions: the first 7 km above the surface, the UTLS region and the middle/upper stratosphere.

The theoretical error estimations are confirmed by comparing the UNAM FTIR product with the Altzomoni FTIR product. We find very good agreement for both data sets concerning total column amounts, UTLS volume mixing ratios and the ratios in the middle/upper stratosphere. A comparison of the lowermost layer is not possible, because the UNAM FTIR data are strongly
20   affected by local O_3 variations in the polluted boundary layer of Mexico City, whereas the Altzomoni FTIR experiment is measuring mainly above this layer. For empirically validating the boundary layer data obtained from the UNAM remote sensing retrievals we use in-situ data obtained at three stations close to the UNAM instrument. We found a good correlation between the UNAM FTIR and the in-situ boundary layer O_3 data and a slope of the linear regression line that is in agreement with the sensitivity as given by the averaging kernels.

25   The Altzomoni FTIR measurements will become very useful in the future, when several years of measurements will be available. The seasonal cycles observed in the total column and the UTLS above Altzomoni are distinct to the cycles as observed at all the other NDACC FTIR stations in the subtropics, mid-latitudes and polar regions. The observation of a UTLS O_3 maximum in late summer instead of late winter and spring (like at other sites) is most probably due to isentropic mixing of O_3 rich air from the high latitudinal stratosphere. This mixing takes place in the northern tropics. In previous studies it has been
30   shown that it is linked to climate patterns like the Asian and North American monsoons and that it is affected by the ENSO phase. Establishing the Altzomoni FTIR as a long-term activity might in the future enable us to investigate the importance of climate patterns, like the North American monsoon or the ENSO, for such stratosphere-troposphere exchange events.

Having two nearby remote sensing measurements, a first one in the boundary layer and a second one just above this layer most of the time, gives the opportunity of creating a combined remote sensing product with improved representativeness of the
35   near surface processes. We have introduced the theory of such combined product and characterise it by calculating averaging

kernels and errors. We are able to prove that the combined FTIR O_3 boundary layer product better represents the near surface variations than the product obtained by a single FTIR experiment. The approach for combining the retrievals of the two FTIR experiments can be applied for any other trace gas in order to reliably detect the Mexico City boundary layer variations of many different trace gases. Nevertheless, for a scientific usage of this remote sensing boundary layer product it would be important

5 to better understand the large bias of 60% with respect to the in-situ data. The bias can be due to systematic errors in the remote sensing data, but also due to the fact that the remote sensing experiments observe different air masses. By measuring O_3 profiles with radiosondes one can detect the same air masses as the remote sensing experiments. In this context, performing in-situ O_3 profile measurements at the UNAM station (radiosonde or balloon) in coincidence to Altzomoni and UNAM FTIR measurements would be very helpful, since it could help understanding the actual systematic error in the boundary layer remote

10 sensing data. With more data and further analysis, our product could be used to quantify the O_3 residual layer and to understand the complex dynamical processes affecting the large variability and high episodes taking place at the surface.

6   Data availability

NDACC FTIR O_3 data of Altzomoni have been stored on the NDACC database: ftp://ftp.cpc.ncep.noaa.gov/ndacc/station/altzomoni/hdf/ftir/. However, please be aware that the data on the NDACC database have been retrieved using a single microwindow at 1000-

15 1005 cm^{-1} (the NDACC standard setting), which is different to the retrieval setting used in this study. In consequence the Altzomoni O_3 data on the NDACC database are slightly different from the here presented O_3 data. The here presented Altzomoni and UNAM O_3 data are so far only available by request to the authors. The RAMA data are available at: www.aire.df.gob.mx/default.php.

Author contributions. E. F. Plaza-Medina, W. Stremme, A. Bezanilla and M. Grutter operated the Altzomoni and UNAM experiments. M. Grutter coordinated the measurement program at both stations. F. Hase, T. Blumenstock and M. Schneider helped in characterising and operating the Altzomoni FTIR instrument. M. Schneider developed the combined UNAM/Altzomoni remote sensing product. E. F. Plaza-Medina prepared this manuscript with important contributions from all the co-authors.

5   *Acknowledgements.* E. F. Plaza-Medina received funding as a Postdoc at CCA/UNAM (becas mujeres 2012 awarded by ICyTDF). M. Schneider was funded by the European Research Council under the European Community's Seventh Framework Programme (FP7/2007-2013) / ERC Grant agreement number 256961. Financial support from CONACYT (239618, 249374, 275239), DGAPA-UNAM (IN109914, IN112216, IN107417) and BMBF (project 01DN12064) is acknowledged for the maintenance and improvements of the FTIR measurements at Altzomoni and UNAM. The RUOA university network of atmospheric observatories (Red Universitaria de Observatorios Atmosféricos,
10   www.ruoa.unam.mx) provided the infrastructure and logistical support for performing the measurements at both sites. Special thanks to D. Flores, A. Rodríguez, H. Soto and O. Torres for their technical assistence and CONANP authorities for hosting the Altzomoni station at the Izta-Popo National Park. The in-situ O_3 data for the stations Pedregal, Santa Ursula and Coyoacan were obtained from the databases of Red Automática de Monitoreo Atmosférico (RAMA), operated by the Ministry of Environment of Mexico City. We acknowledge support by Deutsche Forschungsgemeinschaft and Open Access Publishing Fund of the Karlsruhe Institute of Technology.

References

Barrett, B. S. and Raga, G. B.: Variability of winter and summer surface ozone in Mexico City on the intraseasonal timescale, Atmospheric Chemistry and Physics, 16, 15 359–15 370, doi:10.5194/acp-16-15359-2016, http://www.atmos-chem-phys.net/16/15359/2016/, 2016.

Barthlott, S., Schneider, M., Hase, F., Blumenstock, T., Kiel, M., Dubravica, D., García, O. E., Sepúlveda, E., Mengistu Tsidu, G., Takele Kenea, S., Grutter, M., Plaza, E. F., Stremme, W., Strong, K., Weaver, D., Palm, M., Warneke, T., Notholt, J., Mahieu, E., Servais, C., Jones, N., Griffith, D. W. T., Smale, D., and Robinson, J.: Tropospheric water vapour isotopologue data ($H_2^{16}O$, $H_2^{18}O$ and $HD^{16}O$) as obtained from NDACC/FTIR solar absorption spectra, Earth System Science Data, 9, 15–29, doi:10.5194/essd-9-15-2017, http://www.earth-syst-sci-data.net/9/15/2017/, 2017.

Baumgardner, D., Grutter, M., Allan, J., Ochoa, C., Rappenglueck, B., Russell, L., and Arnott, P.: Physical and chemical properties of the regional mixed layer of Mexico's Megapolis, Atmospheric Chemistry and Physics, 9, 5711–5727, 2009.

Bezanilla, A., Krüger, A., Stremme, W., and Grutter, M.: Solar absorption infrared spectroscopic measurements over Mexico City: Methane enhancements, Atmósfera, 27, 173–183, 2014.

Brasseur, G. P., Orlando, J. J., and Tyndall, G. S.: Atmospheric chemistry and global change, Oxford University Press, New York, USA, 1999.

Dameris, M. and Jöckel, P.: Numerical Modeling of Climate – Chemistry Connections: Recent Developments and Future Challenges, Atmosphere, 4, 132–156, 2013.

Emmons, L. K., Apel, E. C., Lamarque, J.-F., Hess, P. G., Avery, M., Blake, D., Brune, W., Campos, T., Crawford, J., DeCarlo, P. F., Hall, S., Heikes, B., Holloway, J., Jimenez, J. L., Knapp, D. J., Kok, G., Mena-Carrasco, M., Olson, J., O'Sullivan, D., Sachse, G., Walega, J., Weibring, P., Weinheimer, A., and Wiedinmyer, C.: Impact of Mexico City emissions on regional air quality from MOZART-4 simulations, Atmospheric Chemistry and Physics, 10, 6195–6212, doi:10.5194/acp-10-6195-2010, http://www.atmos-chem-phys.net/10/6195/2010/, 2010.

García, O. E., Schneider, M., Redondas, A., González, Y., Hase, F., Blumenstock, T., and Sepúlveda, E.: Investigating the long-term evolution of subtropical ozone profiles applying ground-based FTIR spectrometry, Atmospheric Measurement Techniques, 5, 2917–2931, doi:10.5194/amt-5-2917-2012, http://www.atmos-meas-tech.net/5/2917/2012/, 2012.

Gisi, M., Hase, F., Dohe, S., and Blumenstock, T.: Camtracker: a new camera controlled high precision solar tracker system for FTIR-spectrometers, Atmos. Meas. Tech., 4, 47–54, 2011.

Hase, F.: Improved instrumental line shape monitoring for the ground-based, high-resolution FTIR spectrometers of the Network for the Detection of Atmospheric Composition Change, Atmospheric Measurement Techniques, 5, 603–610, doi:10.5194/amt-5-603-2012, http://www.atmos-meas-tech.net/5/603/2012/, 2012.

Hase, F., Blumenstock, T., and Paton-Walsh, C.: Analysis of the instrumental line shape of high-resolution Fourier transform IR spectrometers with gas cell measurements and new retrieval software, Appl. Optics, 38, 3417–3422, 1999.

Hase, F., Hannigan, J. W., Coffey, M. T., Goldman, A., Höpfner, M., Jones, N. B., Rinsland, C. P., and Wood, S.: Intercomparison of retrieval codes used for the analysis of high-resolution, J. Quant. Spectrosc. Ra., 87, 25–52, 2004.

Hassler, B., Young, P. J., Portmann, R. W., Bodeker, G. E., Daniel, J. S., Rosenlof, K. H., and Solomon, S.: Comparison of three vertically resolved ozone data sets: climatology, trends and radiative forcings, Atmos. Chem. Phys., 13, 5533–5550, 2013.

Hegglin, M. I. and Shepherd, T. G.: Large climate-induced changes in ultraviolet index and stratosphere-to-troposphere ozone flux, Nature Geosci, 2, 687–691, 10.1038/ngeo604, 2009.

IPCC-2013: Summary for Policymakers. In: Climate Change 2013: The Physical Science Basis. Contribution of Working Group I to the Fifth Assessment Report of the Intergovernmental Panel on Climate Change [Stocker, T.F., D. Qin, G.-K. Plattner, M. Tignor, S.K. Allen, J. Boschung, A. Nauels, Y. Xia, V. Bex and P.M. Midgley (eds.)], Cambridge University Press, Cambridge, United Kingdom and New York, NY, USA, 2013.

5   Jacob, D. J. and Winner, D. A.: Effect of climate change on air quality, Atmospheric Environment, 43, 51–63, 2009.

Kohlhepp, R., Ruhnke, R., Chipperfield, M. P., De Mazière, M., Notholt, J., Barthlott, S., Batchelor, R. L., Blatherwick, R. D., Blumenstock, T., Coffey, M. T., Demoulin, P., Fast, H., Feng, W., Goldman, A., Griffith, D. W. T., Hamann, K., Hannigan, J. W., Hase, F., Jones, N. B., Kagawa, A., Kaiser, I., Kasai, Y., Kirner, O., Kouker, W., Lindenmaier, R., Mahieu, E., Mittermeier, R. L., Monge-Sanz, B., Morino, I., Murata, I., Nakajima, H., Palm, M., Paton-Walsh, C., Raffalski, U., Reddmann, T., Rettinger, M., Rinsland, C. P., Rozanov, E., Schneider,

10   M., Senten, C., Servais, C., Sinnhuber, B.-M., Smale, D., Strong, K., Sussmann, R., Taylor, J. R., Vanhaelewyn, G., Warneke, T., Whaley, C., Wiehle, M., and Wood, S. W.: Observed and simulated time evolution of HCl, ClONO$_2$, and HF total column abundances, Atmospheric Chemistry and Physics, 12, 3527–3556, doi:10.5194/acp-12-3527-2012, http://www.atmos-chem-phys.net/12/3527/2012/, 2012.

Molina, L. T., Madronich, S., Gaffney, J. S., Apel, E., de Foy, B., Fast, J., Ferrare, R., Herndon, S., Jimenez, J. L., Lamb, B., Osornio-Vargas, A. R., Russell, P., Schauer, J. J., Stevens, P. S., Volkamer, R., and Zavala, M.: An overview of the MILAGRO 2006 Campaign: Mexico

15   City emissions and their transport and transformation, Atmospheric Chemistry and Physics, 10, 8697–8760, 2010.

Pawson, S., Steinbrecht, W., Charlton-Perez, A., Fujiwara, M., Karpechko, A., Petropavlovskikh, I., Urban, J., and Weber, M.: Update on global ozone: Past, present, and future, Chapter 2 in Scientific Assessment of Ozone Depletion, World Meteorological Organization, Geneva, Switzerland, Global Ozone Research and Monitoring Project, Report No. 55, 2014.

Petersen, A. K., Warneke, T., Lawrence, M. G., Notholt, J., and Schrems, O.: First ground-based FTIR observations of the seasonal variation

20   of carbon monoxide in the tropics, Geophysical Research Letters, 35, L03 813, 2008.

Raga, G. B. and Raga, A. C.: On the formation of an elevated ozone peak in Mexico City, Atmospheric Environment, 34, 4097–4102, 2000.

Ramaswamy, V., Schwarzkopf, M. D., Randel, W. J., Santer, B. D., Soden, B. J., and Stenchikov, G. L.: Anthropogenic and Natural Influences in the Evolution of Lower Stratospheric Cooling, Science, 311, 1138–1141, 2006.

Rees, D., Barnett, J., and Labitzke, K.: Cospar international reference atmosphere: 1986 part II. Middle atmosphere models., Adv. Space

25   Res., 10, 520, 1990.

Rinsland, C. P., Mahieu, E., Zander, R., Jones, N. B., Chipperfield, M. P., Goldman, A., Anderson, J., Russell, J. M., Demoulin, P., Notholt, J., Toon, G. C., Blavier, J.-F., Sen, B., Sussmann, R., Wood, S. W., Meier, A., Griffith, D. W. T., Chiou, L. S., Murcray, F. J., Stephen, T. M., Hase, F., Mikuteit, S., Schulz, A., and Blumenstock, T.: Long-term trends of inorganic chlorine from ground-based infrared solar spectra: Past increases and evidence for stabilization, Journal of Geophysical Research: Atmospheres, 108, doi:10.1029/2002JD003001,

30   http://dx.doi.org/10.1029/2002JD003001, 2003.

Rodgers, C.: Inverse Methods for Atmospheric Sounding: Theory and Praxis, World Scientific Publishing Co., Singapore, 2000.

Rothman, L. S., Gordon, I. E., Barbe, A., Chris Benner, D., Bernath, P. F., Birk, M., Boudon, V., Brown, L. R., Campargue, A., Champion, J.-P., Chance, K., Coudert, L. H., Dana, V., Devi, V. M., Fally, S., Flaud, J.-M., Gamache, R. R., Goldman, A., Jacquemart, D., Kleiner, I., Lacome, N., Lafferty, W. J., Mandin, J.-Y., Massie, S. T., Mikhailenko, S. N., Miller, C. E., Moazzen-Ahmadi, N., Naumenko, O. V.,

35   Nikitin, A. V., Orphal, J., Perevalov, V. I., Perrin, A., Predoi-Cross, A., Rinsland, C. P., Rotger, M., Simecková, M., Smith, M. A. H., Sung, K., Tashkun, S. A., Tennyson, J., Toth, R. A., Vandaele, A. C., and Vander-Auwera, J.: The HITRAN 2008 molecular spectroscopic database, J. Quant. Spectrosc. Radiat. Transfer, 110, 533–572, doi:10.1016/j.jqsrt.2009.02.013, 2009.

Schneider, M. and Hase, F.: Technical Note: Recipe for monitoring of total ozone with a precision of around 1 DU applying mid-infrared solar absorption spectra, Atmospheric Chemistry and Physics, 8, 63–71, doi:10.5194/acp-8-63-2008, http://www.atmos-chem-phys.net/8/63/2008/, 2008.

Schneider, M., Hase, F., and Blumenstock, T.: Water vapour profiles by ground-based FTIR spectroscopy: study for an optimised retrieval and its validation, Atmos. Chem. Phys., 6, 811–830, http://www.atmos-chem-phys.net/6/811/2006/, 2006.

Schneider, M., Hase, F., Blumenstock, T., Redondas, A., and Cuevas, E.: Quality assessment of O_3 profiles measured by a state-of-the-art ground-based FTIR observing system, Atmospheric Chemistry and Physics, 8, 5579–5588, doi:10.5194/acp-8-5579-2008, http://www.atmos-chem-phys.net/8/5579/2008/, 2008.

Senten, C., De Mazière, M., Dils, B., Hermans, C., Kruglanski, M., Neefs, E., Scolas, F., Vandaele, A. C., Vanhaelewyn, G., Vigouroux, C., Carleer, M., Coheur, P. F., Fally, S., Barret, B., Baray, J. L., Delmas, R., Leveau, J., Metzger, J. M., Mahieu, E., Boone, C., Walker, K. A., Bernath, P. F., and Strong, K.: Technical Note: New ground-based FTIR measurements at Ile de La Réunion: observations, error analysis, and comparisons with independent data, Atmospheric Chemistry and Physics, 8, 3483–3508, doi:10.5194/acp-8-3483-2008, http://www.atmos-chem-phys.net/8/3483/2008/, 2008.

Shaw, W. J., Pekour, M. S., Coulter, R. L., Martin, T. J., and Walters, J. T.: The daytime mixing layer observed by radiosonde, profiler, and lidar during MILAGRO, Atmospheric Chemistry and Physics Discussions, 7, 15 025–15 065, doi:10.5194/acpd-7-15025-2007, http://www.atmos-chem-phys-discuss.net/7/15025/2007/, 2007.

Shuckburgh, E., d'Ovidio, F., and Legras, B.: Local Mixing Events in the Upper Troposphere and Lower Stratosphere. Part II: Seasonal and Interannual Variability, Journal of the Atmospheric Sciences, 66, 3695–3706, doi:10.1175/2009JAS2983.1, http://dx.doi.org/10.1175/2009JAS2983.1, 2009.

Stock, Z. S., Russo, M. R., and Pyle, J. A.: Representing ozone extremes in European megacities: the importance of resolution in a global chemistry climate model, Atmos. Chem. Phys., 14, 3899–3912, 2014.

Stolarski, R. S., Waugh, D. W., Wang, L., Oman, L. D., Douglass, A. R., and Newman, P. A.: Seasonal variation of ozone in the tropical lower stratosphere: Southern tropics are different from northern tropics, Journal of Geophysical Research: Atmospheres, 119, 6196–6206, doi:10.1002/2013JD021294, http://dx.doi.org/10.1002/2013JD021294, 2014.

Stremme, W., Ortega, I., and Grutter, M.: Using ground-based solar and lunar infrared spectroscopy to study the diurnal trend of carbon monoxide in the Mexico City boundary layer, Atmospheric Chemistry and Physics, 9, 8061–8078, 2009.

Takele Kenea, S., Mengistu Tsidu, G., Blumenstock, T., Hase, F., von Clarmann, T., and Stiller, G. P.: Retrieval and satellite intercomparison of O_3 measurements from ground-based FTIR Spectrometer at Equatorial Station: Addis Ababa, Ethiopia, Atmospheric Measurement Techniques, 6, 495–509, doi:10.5194/amt-6-495-2013, http://www.atmos-meas-tech.net/6/495/2013/, 2013.

Thompson, A. M., Yorks, J. E., Miller, S. K., Witte, J. C., Dougherty, K. M., Morris, G. A., Baumgardner, D., Ladino, L., and Rappenglück, B.: Tropospheric ozone sources and wave activity over Mexico City and Houston during MILAGRO/Intercontinental Transport Experiment (INTEX-B) Ozonesonde Network Study, 2006 (IONS-06), Atmos. Chem. Phys., 8, 5113–5125, 2008.

Tikhonov, A. N.: SOLUTION OF INCORRECTLY FORMULATED PROBLEMS AND REGULARIZATION METHOD, Doklady Akademii Nauk Sssr, 151, 501, 1963.

Velasco, E., Márquez, C., Bueno, E., Bernabé, R. M., Sánchez, A., Fentanes, O., Wöhrnschimmel, H., Cárdenas, B., Kamilla, A., Wakamatsu, S., and Molina, L. T.: Vertical distribution of ozone and VOCs in the low boundary layer of Mexico City, Atmospheric Chemistry and Physics, 8, 3061–3079, doi:10.5194/acp-8-3061-2008, http://www.atmos-chem-phys.net/8/3061/2008/, 2008.

Viatte, C., Gaubert, B., Eremenko, M., Hase, F., Schneider, M., Blumenstock, T., Ray, M., Chelin, P., Flaud, J.-M., and Orphal, J.: Tropospheric and total ozone columns over Paris (France) measured using medium-resolution ground-based solar-absorption Fourier-transform infrared spectroscopy, Atmospheric Measurement Techniques, 4, 2323–2331, doi:10.5194/amt-4-2323-2011, http://www.atmos-meas-tech.net/4/2323/2011/, 2011.

5 Vigouroux, C., Blumenstock, T., Coffey, M., Errera, Q., García, O., Jones, N. B., Hannigan, J. W., Hase, F., Liley, B., Mahieu, E., Mellqvist, J., Notholt, J., Palm, M., Persson, G., Schneider, M., Servais, C., Smale, D., Thölix, L., and De Mazière, M.: Trends of ozone total columns and vertical distribution from FTIR observations at eight NDACC stations around the globe, Atmospheric Chemistry and Physics, 15, 2915–2933, doi:10.5194/acp-15-2915-2015, http://www.atmos-chem-phys.net/15/2915/2015/, 2015.

Weatherhead, E. C. and Andersen, S. B.: The search for signs of recovery of the ozone layer, Nature, 441, 39–45, doi:10.1038/nature04746, 10 2006.

Zhang, H., Wu, S., Huang, Y., and Wang, Y.: Effects of stratospheric ozone recovery on photochemistry and ozone air quality in the troposphere, Atmos. Chem. Phys., 14, 4079–4086, 2014.
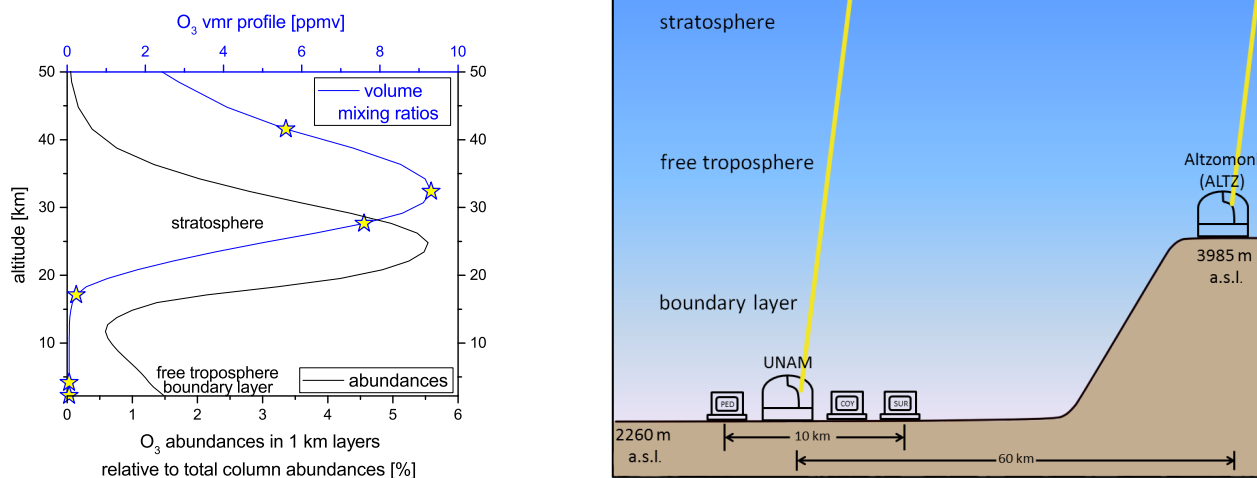
Figure 1. Vertical distribution of O_3 and location of O_3 measuring instrumentation in the surroundings of Mexico City. Left: WACCM version 6 profiles of O_3 volume mixing ratios (blue line) and O_3 abundances (black line) used as a priori for the FTIR retrieval over Mexico City. The yellow stars indicate altitude regions that are analysed in the following sections. Right: schematics indicating the medium resolution FTIR experiment and the three in-situ instruments (at the stations PED, COY and SUR) in Mexico City at and close to UNAM (at about 2.3 km a.s.l.) and the high resolution NDACC FTIR experiment outside the city in Altzomoni (at about 4 km a.s.l.).
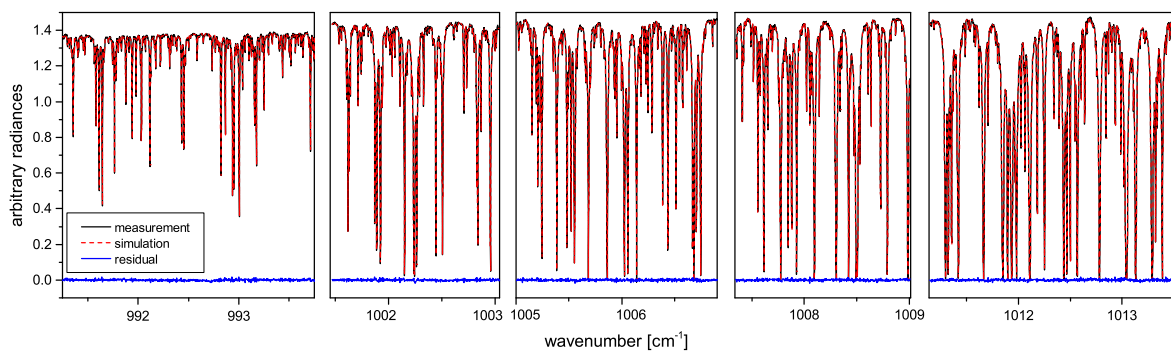
Figure 2. The spectral windows used for the retrievals with the NDACC FTIR instrument at Altzomoni. Shown is an example for a typical measurement (22 March 2013, 17:51 UT; solar elevation: $67.9°$; O_3 slant column: 283 DU). Black line: measurement; red dashed line: simulation; blue line: residual (difference between measurement and simulation).
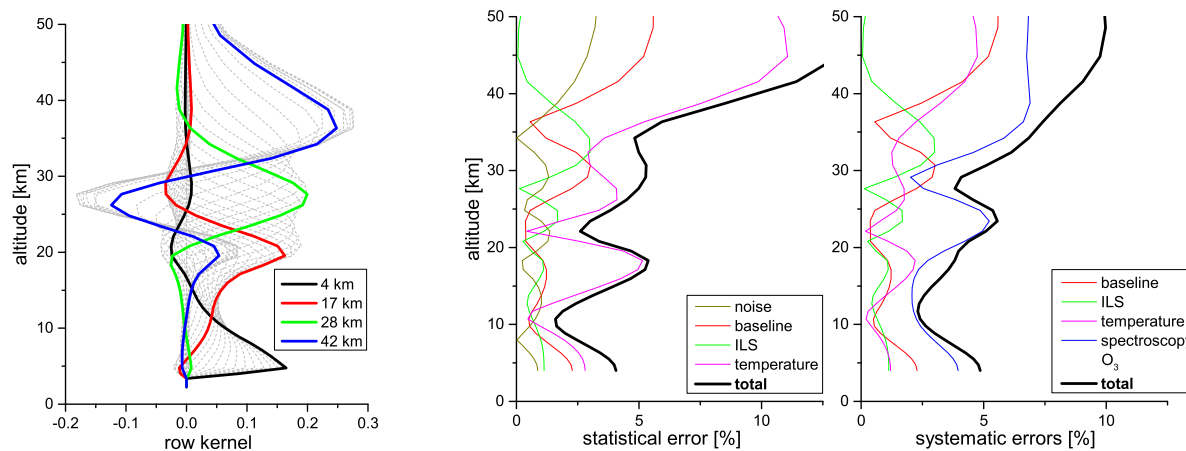
Figure 3. Characterisation of the O_3 volume mixing ratio profiles obtained from the FTIR measurements at Altzomoni as shown in Fig. 2. Left: row averaging kernels, whereby kernels for a few different altitudes are highlighted by different colours. Right: Estimated statistic and systematic errors, whereby the errors resulting from the different uncertainty sources as listed in Table 1 are represented in different colours. The total error is the root-sum-square of the individual errors and is shown as thick black line.
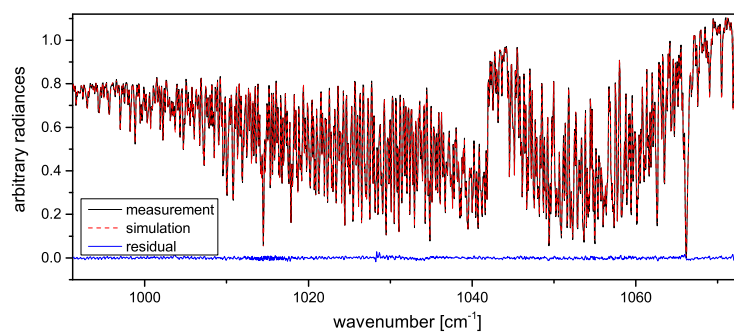
Figure 4. Same as Fig. 2 but for the spectral window used for the retrievals with the FTIR instrument at UNAM. Shown is an example for 22 March 2013, 17:57 UT; solar elevation: 68.2°; O_3 slant column: 285.4 DU.
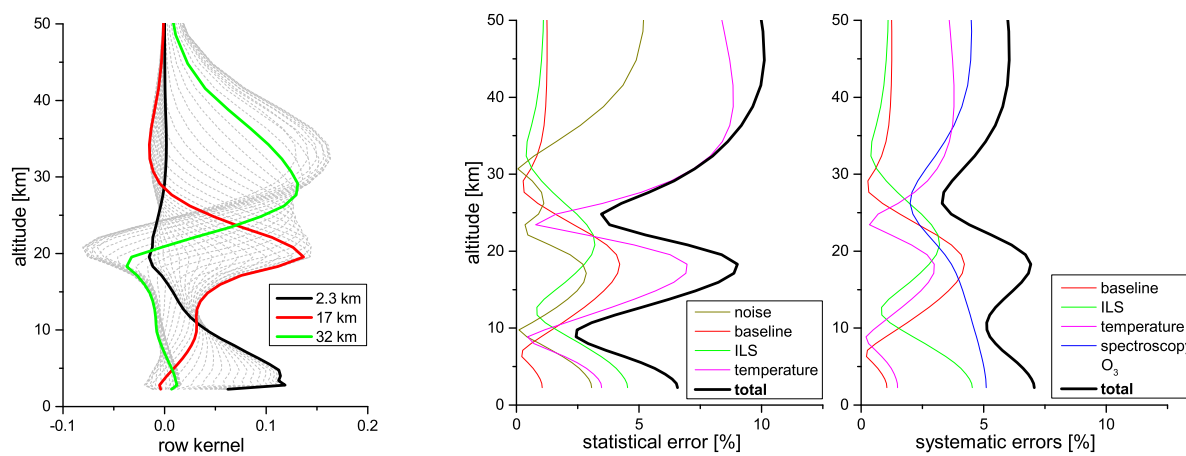
Figure 5. Same as Fig. 3, but for the profiles obtained from the medium resolution FTIR measurements at UNAM as shown in Fig. 4.
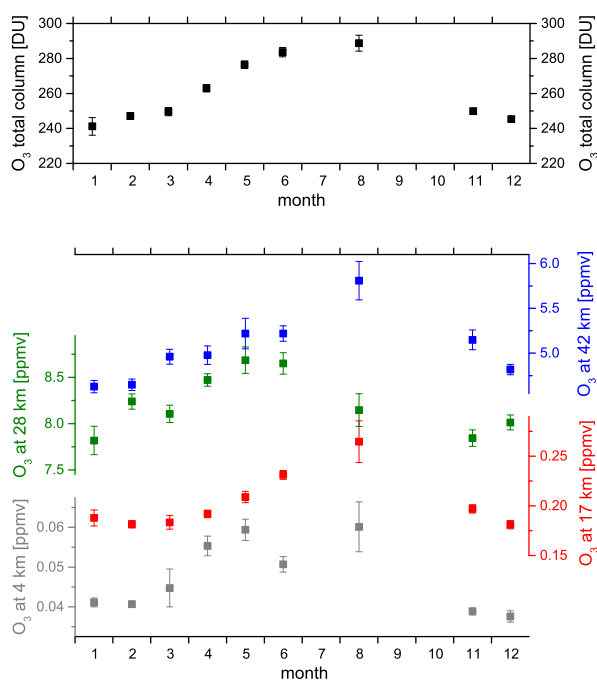
Figure 6. Seasonal O_3 cycles as obtained from the Altzomoni FTIR measurements. Shown are means of all the months with measurements for at least three different days for the altitudes that are highlighted in the kernel plot of Fig. 3 (bottom panel) and for the total column amounts (top panel). Please note that for November-February the monthly means are calculated with data from two different years (2012/13 and 2013/14) for the other months the monthly means are calculated from data of 2013 only.
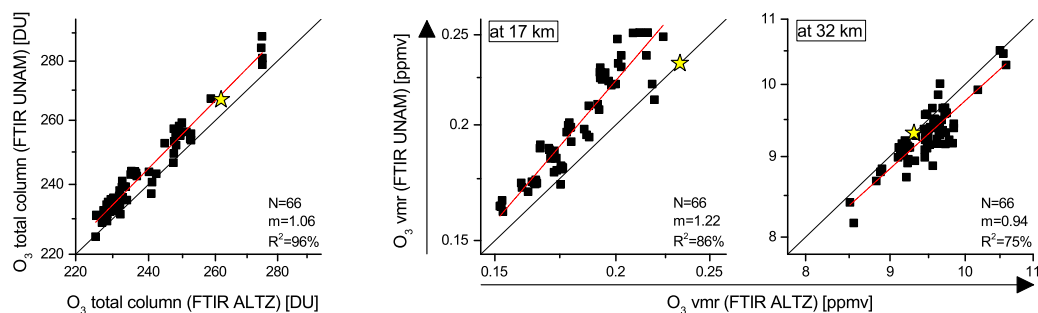
Figure 7. Correlation of O_3 data products obtained from the Altzomoni and UNAM FTIR measurements. The yellow stars represent the a priori values, the black lines are the 1-to-1 diagonals and the red lines are the fitted linear regression lines. Left: total column abundances. Right: volume mixing ratios at 17 and 32 km a.s.l. (in the UNAM kernel plot of Fig. 5 the respective kernels are highlighted by red and green colour). Please note that for this comparison the Altzomoni data have been smoothed by the UNAM averaging kernels according to Eq. (7).
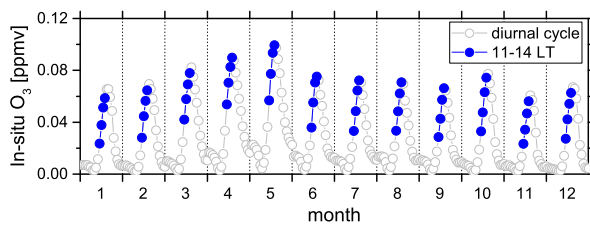
Figure 8. Seasonality of the diurnal cycles of O_3 volume mixing ratios as measured by the three in-situ monitoring stations at about 2.3 km a.s.l. close to UNAM. The blue dots indicate the time frame when FTIR measurements at UNAM have been typically performed.
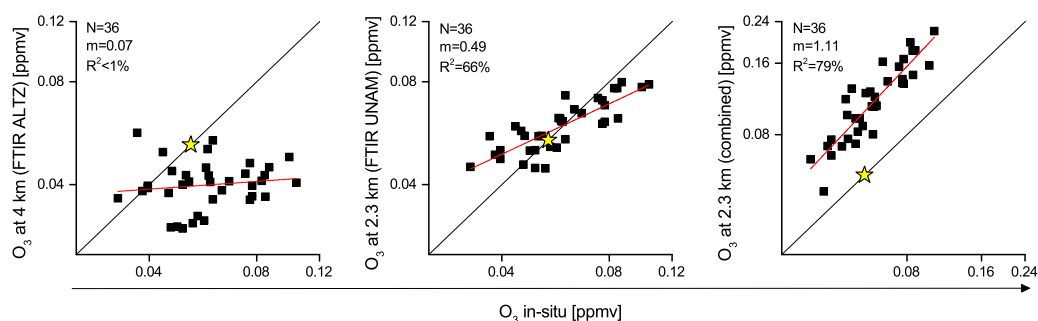
Figure 9. Correlation between O_3 volume mixing ratios measured by the in-situ instruments for the boundary layer of Mexico City and the ratios obtained by the remote sensing experiments. The yellow stars represent the a priori values, the black lines are the 1-to-1 diagonals and the red lines are the fitted linear regression lines. Left: in-situ O_3 versus O_3 obtained from the Altzomoni FTIR measurements for 4 km a.s.l.. Middle: in-situ O_3 versus O_3 obtained from the FTIR UNAM measurements for 2.3 km a.s.l.. Right: in-situ O_3 versus the combined FTIR O_3 product for 2.3 km a.s.l. (calculation according to Eq. 10).
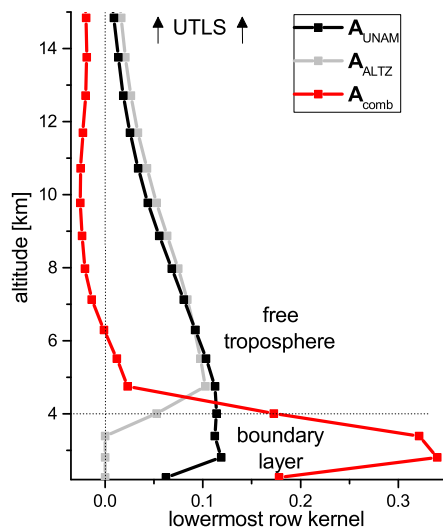
Figure 10. O_3 row kernels for the lowermost altitude of different FTIR products. Black: 2.3 km row kernel for the UNAM product; Grey: 4 km row kernel for the Altzomoni product; Red: 2.3 km row kernel for the combined product.

Table 1. Uncertainties used for the error estimation. The second column gives the uncertainty value and the third column the partitioning between statistical and systematic sources.

Source	Uncertainty	Statistical/Systematic
Measurement noise	0.3% (for Altzomoni)	100/0
	0.5% (for UNAM)	100/0
Baseline (channeling, assuming 4 frequencies: 0.005, 0.2, 1.0, and $3.0\,cm^{-1}$)	0.2%	50/50
Baseline (offset)	1%	50/50
Instrumental line shape (mod. eff. and pha. err.)	5% and 0.1 rad	50/50
Temperature profile	1.5 K (surface - 12.5 km a.s.l.)	70/30
	1.5 K (12.5 - 45 km a.s.l.)	70/30
	6 K (above 45 km a.s.l.)	70/30
Line of sight	$0.2°$	90/10
Solar lines (intensity and ν-scale)	1% and 10^{-6}	80/20
Spectroscopic parameters of O_3	2% (line intensity)	0/100
	5% (pressure broadening)	0/100
Interference with water vapour	100% (atmospheric H_2O)	50/50

Table 2. Estimated errors for the total column abundances of O_3 remote sensing data obtained at Altzomoni and UNAM.

Error source	Altzomoni	UNAM
	Stat. / Sys.	Stat. / Sys.
Measurement noise	0.1% / –	0.4% / –
Baseline	0.9% / 0.9%	1.0% / 1.0%
Instrumental line shape	0.4% / 0.4%	1.0% / 1.0%
Temperature	2.4% / 1.0%	2.5% / 1.1%
Line of sight	0.1% / <0.1%	0.1% / <0.1%
Solar lines	<0.1% / <0.1%	<0.1% / <0.1%
O_3 spectroscopy	– / 2.0%	– / 2.0%
Interference with H_2O	<0.1% / <0.1%	<0.1% / <0.1%
Total	**2.6% / 2.5%**	**2.9% / 2.7%**

Table 3. Estimated errors for the boundary layer O_3 remote sensing (retrieval results for 2.3 km altitude). Listed are statistical and systematic errors of the UNAM product and the combined product.

Error source	UNAM product Stat. / Sys.	Combined product Stat. / Sys.
Measurement noise	3.1% / –	6.8% / –
Baseline	1.0% / 1.0%	14.4% / 14.4%
Instrumental line shape	4.5% / 4.5%	13.1% / 13.1%
Temperature	3.5% / 1.5%	5.5% / 2.4%
Line of sight	0.1% / <0.1%	0.4% / <0.1%
Solar lines	<0.1% / <0.1%	<0.1% / <0.1%
O_3 spectroscopy	– / 5.1%	– / 15.9%
Interference with H_2O	<0.1% / <0.1%	<0.1% / <0.1%
Total	**6.6% / 7.1%**	**21.4% / 25.2%**